

pubs.acs.org/EF Article

Synthesis and Theoretical Modeling of Suitable Co-precipitation Conditions for Producing NMC111 Cathode Material for Lithium-Ion Batteries

Jethrine H. Mugumya, Michael L. Rasche, Robert F. Rafferty, Arjun Patel, Sourav Mallick, Mingyao Mou, Julian A. Bobb, Ram B. Gupta,* and Mo Jiang*



Cite This: https://doi.org/10.1021/acs.energyfuels.2c01805



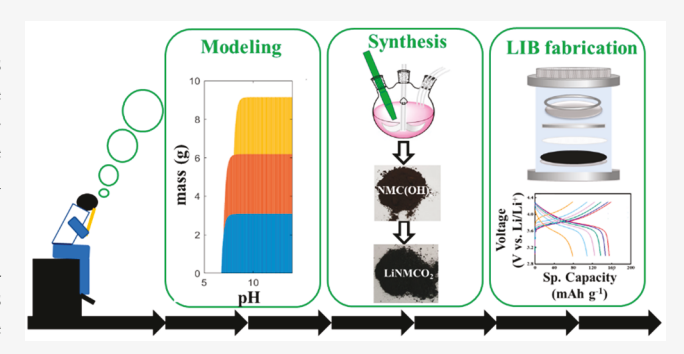
ACCESS

III Metrics & More

Article Recommendations

Supporting Information

ABSTRACT: Lithium nickel manganese cobalt oxide (NMC111) is considered to be one of the most promising cathode materials for commercial lithium-ion battery (LIB) fabrication. Among the various synthesis procedures of NMC111, hydroxide co-precipitation followed by lithiation is the most cost-effective and scalable method. Physical and chemical properties of the co-precipitation product such as yield, particle size, morphology, and tap density, depend upon the various reaction parameters, which include pH, chelating agents, metal salt concentrations, and stirring speed. As a consequence, detailed theoretical and experimental modeling is critically required to not only understand the interdependence between the particle properties and reaction conditions but also



optimize these parameters. In this study, theoretical modeling was performed to analyze the role of various NH₄OH concentrations with varying pH on the yield of the NMC(OH)₂ product. From the experimental findings, it was observed that the product obtained at a pH of 11.5 and NH₄OH concentration of 0.02 M possessed the highest tap density. Three of the hydroxide precursors with different tap density values were chosen to lithiate and were applied for coin cell fabrication. The NMC(OH)₂ precursor with the highest tap density had the highest specific capacity of 155 mAh g⁻¹ at 0.1 C and retained up to 78.6 mAh g⁻¹ at 5 C. The variation of the Li⁺ diffusion coefficient for the three selected materials was also studied using electrochemical impedance analysis.

1. INTRODUCTION

Lithium-ion batteries as a result of their high energy density and long cycling performance ^{1–6} have many applications in various technologies ranging from electric vehicles to electronic gadgets. ^{7–10} To achieve good battery performance, such as rate capability and cycling performance, cathode materials of various compositions and crystal structures should possess the structural robustness to withstand the volume change during lithium ion intercalation and deintercalation. ^{11–14} Among the various cathode materials, layered lithium nickel manganese cobalt oxide (Li[Ni_{0,33}Mn_{0,33}Co_{0,33}]O₂, NMC111) is a promising candidate for commercial applications. The role of nickel in NMC111 is to improve the energy density, while cobalt and manganese provide thermal and structural stability. ^{15–17}

Several synthesis strategies, such as combustion, coprecipitation, sol—gel, and hydrothermal, have been used to produce NMC111 with good tap density and particle size distribution to achieve good battery performance. Hydroxide co-precipitation is the most commonly used method because it is cost-effective and scalable while providing control over the particle morphology and ensuring homogeneous mixing during the synthesis process. Here are many parameters that need to be considered when performing hydroxide co-precipitation

synthesis. These include temperature, metal ion concentrations, chelating agents, and stirring rate; however, the primary focus of this work is to study the effects of the pH and concentration of the chelating agent (ammonium hydroxide) on the quality of the product. ^{29–32} Both parameters play key roles in the precipitation of the NMC(OH)₂ product, where ammonia forms a complex with the metal ions in solution, which then reacts with the hydroxide ions to form metal hydroxide that precipitates out of solution. The pH affects the ability of the metal ions to form the complex with ammonia and the solubility of metal hydroxide in solution. $^{33-35}$

Ammonium hydroxide is the most commonly used chelating agent; however, it easily volatizes to form ammonia gas, which is toxic and an environmental pollutant.³⁶ Research has been conducted with other chelating alternatives such as sodium

Received: May 31, 2022 Revised: August 29, 2022



Table 1. Comparison of NMC111 Synthesized Using Low Ammonia Co-precipitation to Other Values in the Literature

synthesis method	synthesis conditions	precursor size range	initial discharge (mAh g ⁻¹)	voltage window (V)	reference
co-precipitation	$[NH_3]_T = 0.23 M$ pH = 11.5	$2-8~\mu\mathrm{m}$	161 (0.2 C)	2.7-4.3	35
co-precipitation	$[NH_3]_T = 0.57 M$ pH = 11.5	200 nm with 80 nm thickness	166 (0.05 C)	3-4.3	12
co-precipitation	$[NH_3]_T = 0.36 M$ pH = 12.0	$5-20~\mu\mathrm{m}$	163 (32 mA/g)	2.8-4.3	31
co-precipitation	$[NH_3]_T = 0.36 M$ pH = 11.0	9.5–16.7 μ m (majority have 10 μ m)	177 (20 mA/g)	2.8-4.5	22
co-precipitation	$[NH_3]_T = 0.24 M$ pH = 7.5	$5~\mu\mathrm{m}$	162 (0.2 C)	2.8-4.3	42
spray pyrolysis		$6-8 \mu m$ $D_{50} = 6 \mu m$	159.3 (0.1 C)	2.0-4.5	24
co-precipitation	$[NH_3]_T = 1 M$ pH = 10.5	6–18 μm	154.8 (0.1 C)	3-4.3	43
co-precipitation	$[NH_3]_T = -$ pH = 11.0	$0.5-2 \ \mu \text{m}$	155.1 (0.1 C)	2.5-4.6	44
flame-assisted spray pyrolysis		$0.1-0.8~\mu{\rm m}$	153.7 (0.1 C)	2.8-4.25	45
combustion synthesis		500 nm	150.0 (0.05 C)	2.5-4.3	25

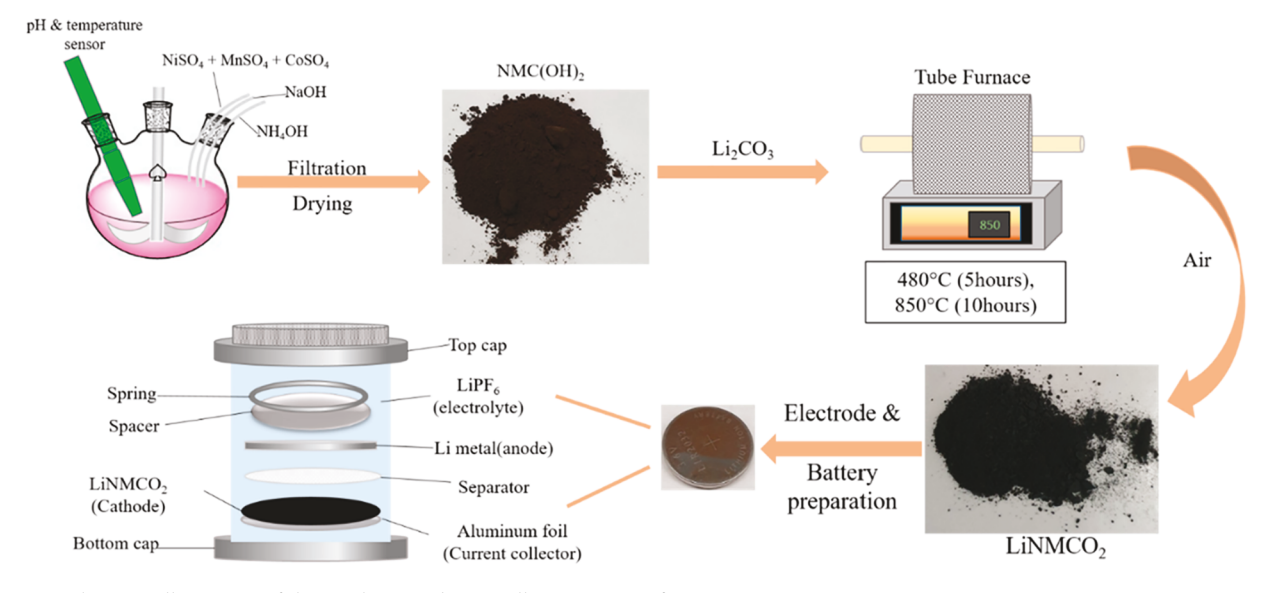


Figure 1. Schematic illustration of the synthesis and coin cell preparation of NMC111.

lactate and oxalic acid.^{37,38} Although the layered metal oxides using these chelating agents do exhibit good performance, ammonium hydroxide in comparison to these alternatives is still the cheaper and more feasible reactant for large-scale production.³⁹ Using low concentrations of ammonia during cathode synthesis is another solution because this will reduce the amount of hazardous gas produced from the process. As such, the objective of this work is to understand the effects of using low concentrations of ammonia during hydroxide co-precipitation on the particle size and tap density, which are key parameters that influence the battery performance.^{40,41} Various research groups have already synthesized NMC111 by different routes to achieve better electrochemical performance. The synthesis condition, particle size, and discharge capacities of a few of such already reported NMC111 are shown in Table 1.

A theoretical model that can predict which pH will provide the highest yield for a given ammonia concentration is proposed. Similar models have been reported in the literature.^{32,35} In the work published by Hua et al., the same constants were used to derive their model. However, the authors only focused on one

ammonia concentration (0.5 M), while in the work published by Shen et al., their main focus was on optimizing the ratio between the metal ion ammonia complex and the hydroxide ion concentration in solution. There are two key differences between the model shown in this work and the works mentioned above: (i) In this work, the goal of the model was to identify experimental conditions that minimize the amount of residual metal ions in solution, thereby optimizing the yield. (ii) The experiments were conducted for multiple ammonia concentrations, and the target composition ratio for the final precursor solid is NMC111. With this model, we can predict optimal pH conditions for low concentrations of ammonia, which would save time and resources needed to optimize the system.³² Experiments are carried out at different ammonia concentrations to assess the model.

2. EXPERIMENTAL SECTION

2.1. Synthesis of $Ni_{1/3}Mn_{1/3}Co_{1/3}(OH)_2$ and Li- $Ni_{1/3}Mn_{1/3}Co_{1/3}O_2$. A 2.0 M transition metal sulfate (MSO₄) solution was prepared by dissolving NiSO₄·6H₂O, CoSO₄·7H₂O, and MnSO₄·

H₂O (all purchased from Sigma-Aldrich) in the desired ratios in deionized (DI) water. Ammonium hydroxide (NH₄OH) solutions, with concentrations in the range of 0.02-0.17 M, and 8.0 M sodium hydroxide (NaOH) were also prepared. NH₄OH solution (50 mL) and 50 mL of DI water were added to a three-neck round-bottom flask under a nitrogen atmosphere and heated to 60 °C. 22,35 MSO₄ solution and the remaining 50 mL of NH₄OH solution were then added simultaneously to the flask under a nitrogen atmosphere (each at a rate of 1 mL min⁻¹), while NaOH is added to maintain the pH of the mixture, as shown in Figure 1. The mixture is allowed to ripen for 12 h with a stirring rate of 1000 rpm. The resulting mixture is then washed and filtered until the pH is reduced to 7.0 and dried at 110 °C overnight. The dried precursor material $[NMC(OH)_2]$ was then mixed with 10 wt % excess lithium carbonate in a pestle and mortar then heated in air to a temperature of 480 $^{\circ}$ C for 5 h. The resulting sample was then allowed to cool to room temperature and then ground again before it is calcined at a temperature of 850 °C for 10 h to produce lithium nickel manganese cobalt oxide (NMC111).

2.2. Material Characterization. The morphology of the precursor samples was analyzed using scanning electron microscopy (SEM, Hitachi SU-70 FE-SEM) operated at 10 kV. The X-ray diffraction (XRD) patterns of the precursor and lithiated samples were analyzed using XRD (Empyrean multipurpose X-ray diffractometer) with a Cu $K\alpha$ radiation source of wavelength, 1.5406 Å. The XRD patterns were collected on a 2θ range of $10-80^{\circ}$. Further analysis of the patterns was performed using the Rietveld refinement method on the High Score Software from Panalytical. The surface areas of the samples were measured using the Brunauer-Emmett-Teller (BET) method on a Micrometrics Tristar II plus analyzer with nitrogen gas adsorption. Tap density was measured using Autotap from Quantachrome Instruments. The chemical composition of the samples was measured using inductively coupled plasma optical emission spectrometry (ICP-OES, 5110, Agilent Technologies). Particle size analysis was conducted using Sympatec HELOS from Sympatec GmbH.

2.3. Electrochemical Measurements. The cathode was prepared by uniformly mixing the selected active materials (NMC111), carbon black (Super P conductive carbon black, MSE Supplies), and polyvinylidene difluoride (PVDF, HSV 900) binder in N-methyl pyrrolidone (NMP, 99.5% anhydrous, Sigma-Aldrich) solvent in a weight ratio of 8:1:1. The slurry was then cast on battery-grade aluminum foil using the doctor blade technique and then dried at 130 °C for 12 h. The loading of the active material was 3–4 mg cm⁻². The coin cells were then assembled in an argon-filled glovebox using the prepared cathode, lithium metal as the anode, Celgrade 2340 trilayer microporous membrane as the separator, and 1.0 M LiPF₆ in ethylene carbonate/dimethyl carbonate [EC/DMC = 50:50 (v/v), Sigma-Aldrich] as the electrolyte. The galvanostatic charge/discharge at different current rates (1 C = 200 mAh g⁻¹) and electrochemical impedance spectroscopy (EIS) were performed. Charge/discharge was carried out in a voltage range of 3.0–4.3 V (versus Li/Li⁺) using a MTI battery test cycler. EIS was performed after 5 discharge-charge cycles at 1 C with an amplitude of 5 mV within a frequency range from 100 kHz to 10 mHz using a Gamry potentiostat interface 5000E. All electrochemical tests were conducted at room temperature.

3. RESULTS AND DISCUSSION

3.1. Theoretical Modeling and Analysis of NMC(OH)₂ Precursor Solid Composition. The starting set of equations used to derive this model can be found in eqs S1–S9 of the Supporting Information. Assuming the total ammonia concentration is the only known quantity, we can use eqs S1–S4 of the Supporting Information to rewrite the balances (eqs S6–S9 of the Supporting Information) and obtain the following equations:

$$[NH_3]_T = [NH_3] + \frac{K_A[NH_3]}{K_w 10^{PH}} + \sum_{i=1}^6 iK_{niA,i}[Ni^{2+}][NH_3]^i$$

$$+ \sum_{i=1}^6 iK_{coA,i}[Co^{2+}][NH_3]^i + K_{mnA,1}[Mn^{2+}][NH_3]$$

$$+ 2K_{mnA,2}[Mn^{2+}][NH_3]^2$$
(1)

$$[Ni]_{T} = [Ni^{2+}] + \sum_{i=1}^{6} K_{niA,i}[Ni^{2+}][NH_{3}]^{i} + \sum_{i=1}^{3} K_{nih,i}[Ni^{2+}](K_{w}10^{pH})^{i}$$
(2)

$$[\text{Co}]_{\text{T}} = [\text{Co}^{2+}] + \sum_{i=1}^{6} K_{\text{coA},i} [\text{Co}^{2+}] [\text{NH}_{3}]^{i} + \sum_{i=1}^{4} K_{\text{coh},i} [\text{Co}^{2+}] (K_{\text{w}} 10^{\text{pH}})^{i}$$
(3)

$$\begin{split} [Mn]_{T} &= [Mn^{2+}] + K_{mnA,1}[Mn^{2+}][NH_{3}] + K_{mnA,2}[Mn^{2+}][NH_{3}]^{2} \\ &+ K_{mnh,1}[Mn^{2+}](K_{w}10^{pH}) + K_{mnh,3}[Mn^{2+}](K_{w}10^{pH})^{3} \end{split} \tag{4}$$

Using eq S5 of the Supporting Information, we can express each metal ion term, $[M^{2+}]$, in eqs 1–4 as a function of pH.

$$[M^{2+}] = \frac{K_{\text{spmh}}}{[OH^{-}]^{2}} = \frac{K_{\text{spmh}}}{K_{w}^{2} 10^{2pH}}$$
 (5)

We can factor out the metal ion terms in eqs 2–4 and substitute the expression from eq 5.

$$[NH_{3}]_{T} = [NH_{3}] + \frac{K_{A}[NH_{3}]}{[(K_{w}10^{pH})^{2}]} + \sum_{i=1}^{6} iK_{niA,i} \left[\frac{K_{spnih}}{(K_{w}10^{pH})^{2}} \right] [NH_{3}]^{i}$$

$$+ \sum_{i=1}^{6} iK_{coA,i} \left[\frac{K_{spcoh}}{(K_{w}10^{pH})^{2}} \right] [NH_{3}]^{i} + K_{mnA,1} \left[\frac{K_{spmnh}}{(K_{w}10^{pH})^{2}} \right] [NH_{3}]$$

$$+ 2K_{mnA,2} \left[\frac{K_{spmnh}}{(K_{w}10^{pH})^{2}} \right] [NH_{3}]^{2}$$
(6)

$$[Ni]_{T} = \left[\frac{K_{\text{spnih}}}{(K_{\text{w}}10^{\text{pH}})^{2}}\right] \left\{1 + \sum_{i=1}^{6} K_{\text{niA},i} [NH_{3}]^{i} + \sum_{i=1}^{3} K_{\text{niH},i} [K_{\text{w}}10^{\text{pH}}]^{i}\right\}$$
(7)

$$[\text{Co}]_{\text{T}} = \left[\frac{K_{\text{spcoh}}}{(K_{\text{w}} 10^{\text{pH}})^2}\right] \left\{1 + \sum_{i=1}^{6} K_{\text{coA},i} [\text{NH}_3]^i + \sum_{i=1}^{4} K_{\text{coH},i} [K_{\text{w}} 10^{\text{pH}}]^i\right\}$$
(8)

$$[Mn]_{T} = \left[\frac{K_{\text{spmnh}}}{(K_{w}10^{\text{pH}})^{2}}\right] \{1 + K_{\text{mnA,1}}[NH_{3}] + K_{\text{mnA,2}}[NH_{3}]^{2} + K_{\text{mnH,1}}[K_{w}10^{\text{pH}}] + K_{\text{mnH,3}}[K_{w}10^{\text{pH}}]^{3}\}$$
(9)

With the expansion of the ammonia balance in eq 6 and collection of like terms, a polynomial function (eq 10) of the free ammonia concentration, ($[NH_3]$), is obtained.

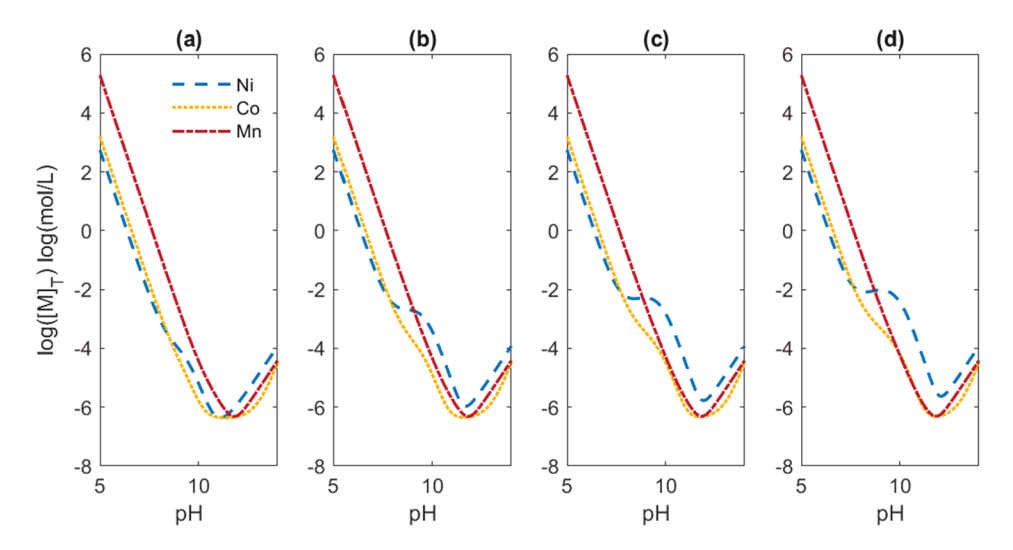


Figure 2. Concentrations of residual metal ions (Ni, Mn, and Co) in solutions at different pH values for ammonia concentrations: (a) 0.02 M, (b) 0.09 M, (c) 0.13 M, and (d) 0.17 M.

Table 2. Experimental Conditions Synthesized with the Optimized Cationic Ratio (0.58 M for Ni, 0.76 M for Mn, and 0.64 M for Co) and ICP Analysis of the Resulting NMC(OH)₂

sample	$[NH_3]_T(M)$	pH optimum for $[NH_3]_T$	experimental pH	Ni/Mn/Co ratio in solid NMC(OH) $_2$ [ICP data] (mol %)	experimental yield (%)
CS-05	0.02	11.5	11.0 ± 0.1	32.5:34.0:33.4	87
CS-06	0.02	11.5	11.5 ± 0.1	32.8:33.4:33.2	100
CS-07	0.02	11.5	12.0 ± 0.1	43.4:27.6:28.9	98
CS-08	0.09	11.7	11.0 ± 0.1	34.0:33.7:32.1	100
CS-09	0.09	11.7	11.5 ± 0.1	34.8:30.3:34.2	98
CS-10	0.09	11.7	12.0 ± 0.1	32.8:33.0:33.3	100
CS-11	0.09	11.7	11.8 ± 0.1	33.3:34.3:33.2	98
CS-12	0.13	11.9	11.8 ± 0.1	32.9:34.1:32.2	99
CS-13	0.17	12.0	11.8 ± 0.1	32.4:33.8:33.0	99

$$\begin{split} [\mathrm{NH_{3}}]_{\mathrm{T}} &= \left(1 + \frac{K_{\mathrm{A}}}{K_{\mathrm{w}} 10^{\mathrm{pH}}} + \frac{K_{\mathrm{niA,1}} K_{\mathrm{spnih}}}{K_{\mathrm{w}}^{2} 10^{2\mathrm{pH}}} + \frac{K_{\mathrm{coA,1}} K_{\mathrm{spcoh}}}{K_{\mathrm{w}}^{2} 10^{2\mathrm{pH}}} \right. \\ &+ \frac{K_{\mathrm{mnA,1}} K_{\mathrm{spmnh}}}{K_{\mathrm{w}}^{2} 10^{2\mathrm{pH}}} \Big[[\mathrm{NH_{3}}] + \left(\frac{2K_{\mathrm{niA,2}} K_{\mathrm{spnih}}}{K_{\mathrm{w}}^{2} 10^{2\mathrm{pH}}} + \frac{2K_{\mathrm{coA,2}} K_{\mathrm{spcoh}}}{K_{\mathrm{w}}^{2} 10^{2\mathrm{pH}}} \right. \\ &+ \frac{2K_{\mathrm{mnA,2}} K_{\mathrm{spmnh}}}{K_{\mathrm{w}}^{2} 10^{2\mathrm{pH}}} \Big[[\mathrm{NH_{3}}]^{2} + \left(\frac{3K_{\mathrm{niA,3}} K_{\mathrm{spnih}}}{K_{\mathrm{w}}^{2} 10^{2\mathrm{pH}}} + \frac{3K_{\mathrm{coA,3}} K_{\mathrm{spcoh}}}{K_{\mathrm{w}}^{2} 10^{2\mathrm{pH}}} \right) \Big] \\ &= [\mathrm{NH_{3}}]^{3} + \left(\frac{4K_{\mathrm{niA,4}} K_{\mathrm{spnih}}}{K_{\mathrm{w}}^{2} 10^{2\mathrm{pH}}} + \frac{4K_{\mathrm{coA,4}} K_{\mathrm{spcoh}}}{K_{\mathrm{w}}^{2} 10^{2\mathrm{pH}}} \right) [\mathrm{NH_{3}}]^{4} \\ &+ \left(\frac{5K_{\mathrm{niA,5}} K_{\mathrm{spnih}}}{K_{\mathrm{w}}^{2} 10^{2\mathrm{pH}}} + \frac{5K_{\mathrm{coA,5}} K_{\mathrm{spcoh}}}{K_{\mathrm{w}}^{2} 10^{2\mathrm{pH}}} \right) [\mathrm{NH_{3}}]^{5} + \left(\frac{6K_{\mathrm{niA,6}} K_{\mathrm{spnih}}}{K_{\mathrm{w}}^{2} 10^{2\mathrm{pH}}} + \frac{6K_{\mathrm{coA,6}} K_{\mathrm{spcoh}}}{K_{\mathrm{w}}^{2} 10^{2\mathrm{pH}}} \right) [\mathrm{NH_{3}}]^{6} \end{aligned}$$

For a given total ammonia concentration, eq 10 can be solved independently and quickly by extracting the single positive, real root of the polynomial using software like MATLAB. The resulting solution can then be used to calculate the residual metal ion concentrations (eqs 7-9), and the results are shown in Figure 2.

Experiments were carried out initially with equal concentrations of the metal ions in the starting sulfate solution (0.67 M for NiSO₄, 0.67 M for CoSO₄, and 0.67 M for MnSO₄). ICP analysis of the synthesized metal hydroxide precursors was then conducted, and the results are shown in Table S2 of the Supporting Information. It was found that, for some of the conditions, the metal ion composition in the final precursor solid

did not have a uniform ratio. This is a result of the reaction conditions when using a low ammonia concentration for hydroxide co-precipitation. With low ammonia concentrations, the reaction kinetics are very fast because the metal ions are more likely to react with the hydroxide ions rather than forming the metal ion complexes with ammonia first, leading to precursor samples with non-uniform chemical compositions.⁴⁶ Because the target metal ion composition of the metal hydroxide precursor is the cationic ratio 1:1:1, the starting metal ion concentrations of the transition metal sulfate solution were adjusted using eq 11 and the ICP composition data from Table S2 of the Supporting Information. Additional experiments were carried out to optimize the starting ratios of the metal ions to obtain a metal hydroxide precursor with the target cationic ratio of 1:1:1. The starting metal ion concentrations were optimized to 0.58 M for NiSO₄, 0.64 M for CoSO₄, and 0.76 M for MnSO₄ for a solution with a 2 M total concentration.

$$\frac{\text{MSO}_4 \text{ mass}}{\text{actual mol }\% \text{ in NMC(OH)}_2} \times \text{target mol }\%$$
(11)

Experiments were conducted to evaluate the validity of the theoretical model in predicting the pH value to result in the highest yield for a given ammonia concentration. From results in Table S2 of the Supporting Information and Table 2, it is observed that, for ammonia concentrations of 0.2 M (CS-01–CS-04) and 0.02 M (CS-05–CS-07), the highest yield was obtained at the pH value closest to the optimal pH predicted by the model. However, with the ammonia concentration of 0.09 M

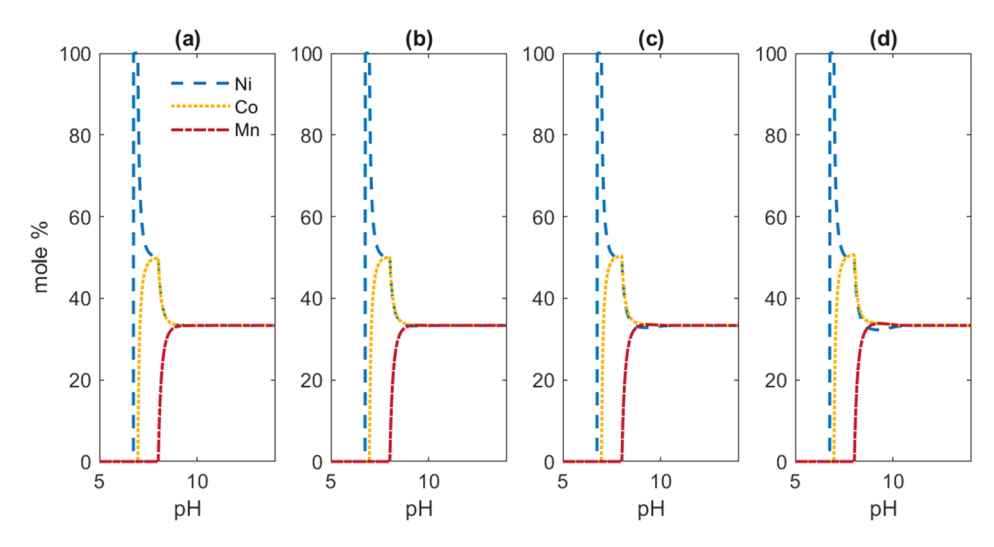
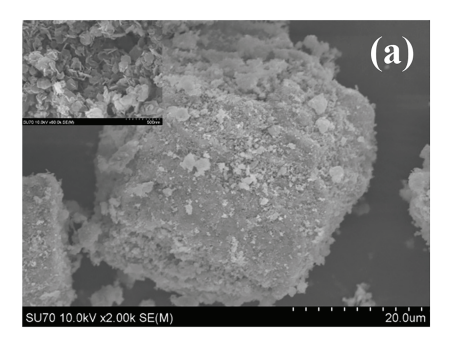


Figure 3. Plots showing the model predictions for composition of the precursor solid for different pH values at different ammonia concentrations: (a) 0.02 M, (b) 0.09 M, (c) 0.13 M, and (d) 0.17 M.



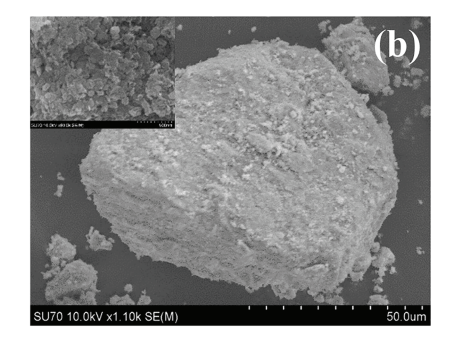


Figure 4. SEM images of the secondary particles of the NMC(OH)₂ precursor samples, with the primary particle images displayed in the insets: (a) pH below 11.5 and (b) pH between 11.5 and 12.0.

(CS-08–CS-11), the results show that the yield is unaffected by the pH. From these results, it can be seen that the model prediction was accurate for most of the ammonia concentrations.

For the model predicted with the optimized starting cationic ratio, the precursors would have a composition of 29.3 mol % Ni, 38.4 mol % Mn, and 32.3 mol % Co for all synthesis conditions and a yield of 99.9%. The predicted yield and composition data were obtained from Figure 3 and Figure S1 of the Supporting Information. Composition analysis of the precursor samples is shown in Table 2, and for most synthesis conditions, the resulting NMC(OH)₂ had an equal amount of each metal ion, except sample CS-07, where the ammonia concentration was 0.02 M at a pH of 12. This is because nickel is more likely to form a complex with ammonia at higher pH than cobalt and manganese; hence, the resulting NMC(OH)₂ had a higher amount of nickel than cobalt and manganese.³³ From samples CS-11 to CS-13, it was observed that increasing the ammonia concentration while maintaining a constant pH led to a decrease in the amount of nickel that precipitates out of solution. This is because nickel is more likely to remain as a metal ammine complex with a higher amount of ammonia in solution, as indicated by the "hump" in the nickel plot in Figure 2. This phenomenon is also discussed in the literature. 32,33 All conditions resulted in a high product yield (>80%), and those samples synthesized at the optimal pH or higher than the optimal pH gave 100% yield. Increasing the pH generally led to a

2% change in the yield, while changing the ammonia concentration only led to a 1% increase.

3.2. Physical and Morphological Characterizations. Figure 4 shows the SEM images of the metal hydroxide precursor, and from these images, it can be deduced that platelike primary particles were formed first and then agglomerated to form secondary particles. Primary particles generally had a vertical orientation in precursors that were synthesized at a pH value below 11.5, while metal hydroxides synthesized at a pH value higher than 11.5 had primary particles in the horizontal orientation. The orientation of primary particles had an impact on the tap density. Precursor samples with primary particles that agglomerated in the vertical orientation had much more space between particles, resulting in samples with a tap density less than 1 g mL⁻¹. Samples with primary particles that agglomerated in the horizontal orientation had minimal space between primary particles, which resulted in precursors with a higher tap density. 41 These results are shown in Table 3, where precursor samples synthesized at a pH higher than 11.5 had tap densities greater than 1 g mL⁻¹.

From the particle size analysis data shown in Figure S2 of the Supporting Information, most of the precursor samples are observed to have a size distribution ranging from 1 μ m (D_{10}) to around 50–60 μ m, with the peak value closer to 50–60 μ m (D_{90}). Because the peak value is closer to the D_{90} size distribution, it is chosen as the value for comparison between the samples. The secondary particle sizes of the different samples

Table 3. Size and Tap Density of the Precursor Samples

sample name	tap density (g m L^{-1})	secondary particle size, D_{90} (μ m)
CS-05	0.91	62.47
CS-06	1.14	66.88
CS-07	1.06	66.63
CS-08	0.63	50.66
CS-09	0.93	55.54
CS-10	1.07	66.26
CS-11	1.11	53.83
CS-12	1.11	53.88
CS-13	1.11	53.85

are mainly between 50 and 60 μ m. An increase in the secondary particle size was observed with an increase in pH, while increasing the ammonia concentration at the same pH had no impact on the particle size. Small peaks around the 1 μ m mark in the size distribution plot (Figure S2 of the Supporting Information) indicate the possibility of multistage aggregation, where initially the primary particles agglomerate to only form secondary particles of a 1 μ m size, and these agglomerates later aggregate further to form secondary particles of larger sizes. ⁴⁷ In summary, increasing the pH led to an increase in tap density, while an increase in the ammonia concentration had no impact on the secondary particle size or tap density.

Figure 5 shows the XRD spectra of all of the precursor samples, and when the patterns are compared to the typical

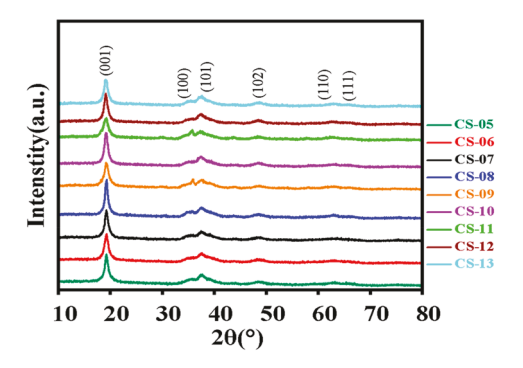


Figure 5. XRD patterns of precursor samples (metal hydroxides) of CS-05-CS-13.

pattern of a metal hydroxide precursor [Joint Committee on Powder Diffraction Standards (JCPDS) card number 14-0117], the peaks in the standard XRD spectra are more prominent. This is because the patterns in Figure 5 are from samples that have both the hydroxide and oxy-hydroxide phases present.⁴⁸ This mixture of phases is due to the oxidation of the cobalt ion from Co²⁺ to Co³⁺ and the manganese cation from Mn²⁺ to Mn⁴⁺ during the drying stage of the metal hydroxide in air after filtration. This oxidation also results in the color change of the precursor from light pink to dark brown, as shown in Figure 1. However, this oxy-hydroxide impurity phase is removed during calcination, as shown by the absence of impurity peaks in the XRD patterns of the lithiated samples in Figure 6.

3.3. Electrochemical Performance. Among the nine precursor samples, three were chosen for lithiation based on the difference in tap density, and those samples are CS-05, CS-06, and CS-08. Figure 6 shows the XRD patterns of the three lithiated samples. All of the samples showed an impurity-free single-phase material that could be indexed to a hexagonal α -NaFeO₂-type structure $(R\overline{3}m)$. $^{47,49-51}$ There was clear splitting

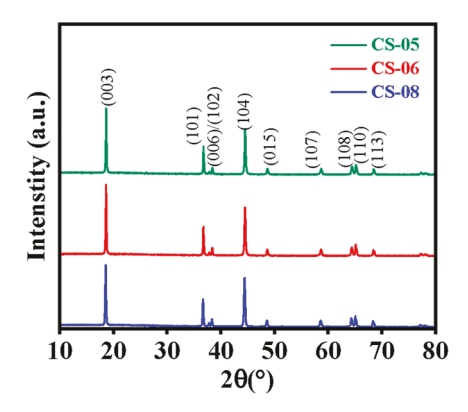


Figure 6. XRD patterns of NMC111 for samples CS-05, CS-06, and CS-08

observed between the (006)/(102) and (108)/(110) peaks, which indicated that the samples had a well-defined layered hexagonal structure. The XRD patterns were further analyzed using Rietveld refinement, and the results are shown in Table 4. The c/a ratio calculated from the lattice parameters of the NMC111 powders is of a high value, which is ideal for layered compounds because it also indicates a good hexagonal structure. The intensity ratios of the (003)/(104) peaks for all three samples are greater than 1.2, which shows there is minimal Li/Ni mixing, which is an indicator of good electrochemical performance. A higher intensity ratio of $I_{(003)}/I_{(104)}$ indicates a low degree of cation mixing, which is essential for facile lithium ion transfer during cycling. S3,54

Figure 7 shows the charge-discharge performance of the three materials (CS-05, CS-06, and CS-08) within the voltage window of 3.0-4.3 V (versus Li/Li⁺). In all three cases, only one discharge plateau is observed, and it corresponds to the Li⁺ intercalation into the cathode material. The electrochemical performance within a fixed voltage window largely depends upon the quality of the cathode materials, which are determined by various parameters, like tap density, particle size, and extent of Li⁺/Ni²⁺ mixing. ^{22,32,55} In our case, CS-06 with the highest tap density of 1.37 g mL⁻¹ and the highest $I_{(003)}/I_{(104)}$ of 1.45 shows a higher specific capacity of 155 mAh g^{-1} at the C rate of 0.1 C compared to CS-05 and CS-08. The material also had specific capacities of 146.7, 136.85, 123.97, 108.59, and 78.64 mAh g⁻¹ at the current rates of 0.2, 0.5, 1, 2, and 5 C, respectively (Figure 7a). On the other hand, CS-05 with a tap density of 1.17 g mL^{-1} but slightly lower $I_{(003)}/I_{(104)}$ ratio of 1.44 achieves a specific capacity of 150 mAh g^{-1} at 0.1 C and retained up to 73.08 mAh g⁻¹ at 5 C (Figure S3a of the Supporting Information). CS-08 with both the lowest tap density (0.89 g mL⁻¹) and $I_{(003)}/I_{(104)}$ ratio (1.27) had the lowest specific capacity of 142.12 mAh g at 0.1 C; however, it retains up to 83.094 mAh g⁻¹ at 5 C, which is better in comparison to the other two materials (Figure S3b of the Supporting Information). It is also observed that the polarization of all of the electrodes increased with the increase in the C rate, which is reflected through the increased chargedischarge plateau gap. Figure 7b compares the electrochemical charge storage performance of the three materials at 0.1 C, and it is observed that CS-08 is showing a greater charge-discharge plateau gap (0.28 V) compared to the other two materials (0.19 V). The rate capability plots of all three materials are given in Figure 7c. In all of the cases, it was observed that the specific capacity was decreasing with an increasing current rate, and around 93-100% of the initial value was achieved once the

Table 4. Lattice Parameters, Tap Density, and Specific Surface Area of Calcined Samples

sample name	$I_{(003)}/I_{(104)}$	R factor	a (Å)	c (Å)	c/a	unit cell volume (\mathring{A}^3)	surface area $(m^2 g^{-1})$	particle size, $D_{90}~(\mu\mathrm{m})$	NMC111 tap density $(g \text{ mL}^{-1})$
CS-05	1.44	0.4606	2.861	14.243	4.98	100.942	7.19	43.34	1.17 (±0.01)
CS-06	1.45	0.4303	2.860	14.238	4.98	100.829	6.00	57.21	$1.37 (\pm 0.05)$
CS-08	1.27	0.465	2.859	14.236	4.98	100.774	7.16	44.19	$0.89 (\pm 0.02)$

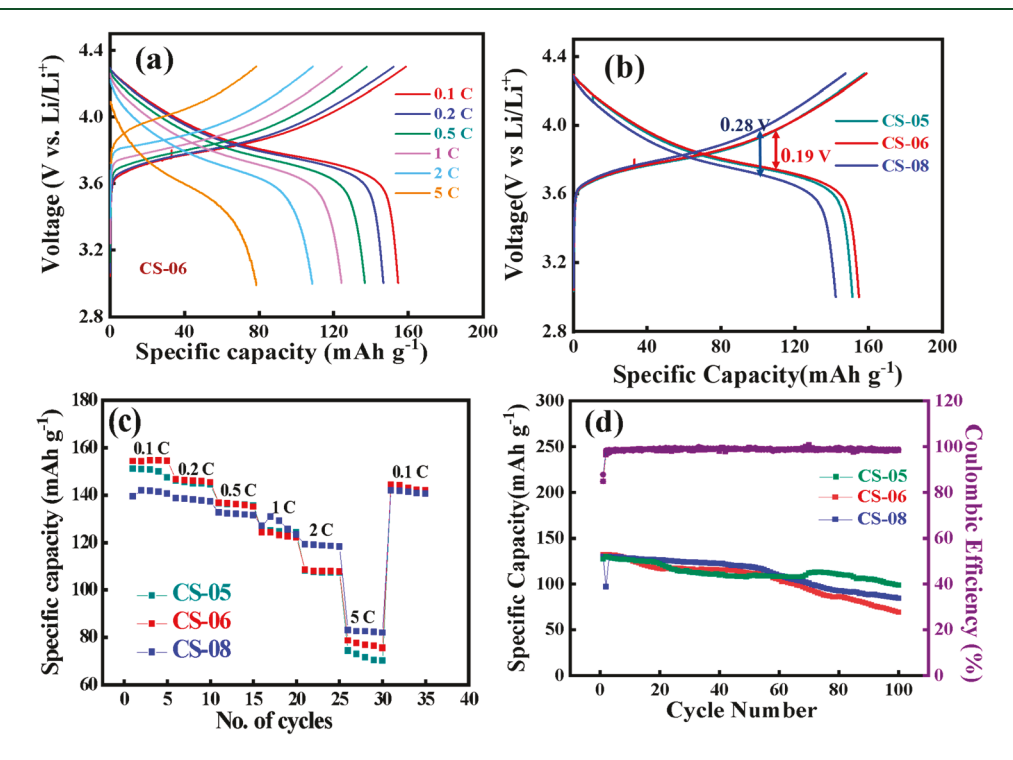


Figure 7. (a) Galvanostatic charge—discharge profiles at different C rates for CS-06. Comparative (b) charge—discharge profile at 0.1 C, (c) rate capability plots, and (d) cycling performance profile of CS-05, CS-06, and CS-08.

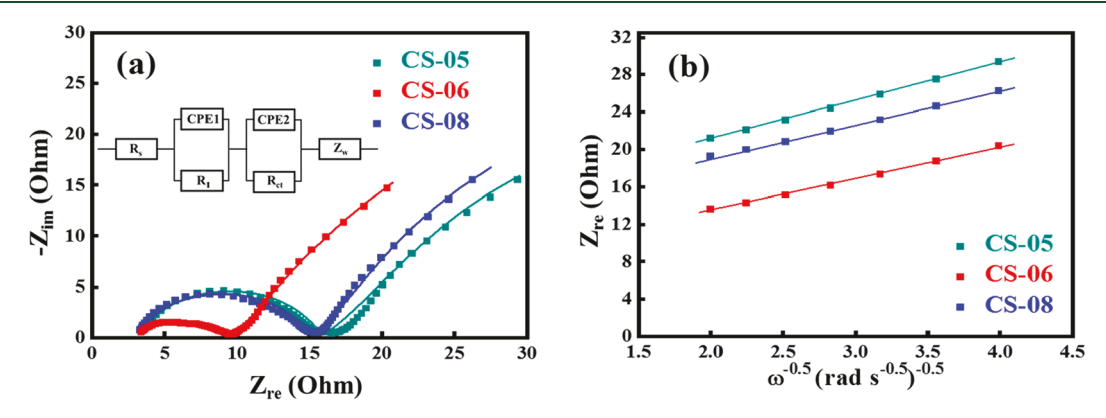


Figure 8. (a) Nyquist and (b) $Z_{\rm re} - \omega^{-0.5}$ plots for CS-05, CS-06, and CS-08. The equivalent circuit is given in the inset of panel a.

current rate was decreased to 0.1 C again. This signifies good retention of the electrochemical performance. The initial columbic efficiency values for three selected materials are observed to be 90–100% at all of the current rates (Table S3 of the Supporting Information), which further proves that assynthesized NMC111 samples are efficient LIB cathode materials. The cycling performance is one of the key parameters that decides the commercial success of the material as a battery electrode. To understand the effect of the nature of the cathode material on the stability of the electrode, the cycling charge—discharge experiment was performed within the voltage window of 3.0–4.3 V (versus Li/Li⁺) for 100 cycles at the current rate of

1 C. Figure 7d shows that the charge storage performance of all of the three materials are decreasing by the course of potential-induced cycling. The charge—discharge curves at different cycle numbers for the three materials are shown in Figure S4 of the Supporting Information. To analyze the fate of the cathode materials after cycling, the post-cycling SEM analysis was conducted and shown in Table S4 of the Supporting Information. From the SEM images, it was observed that, for CS-05, although some of the particles are cracked after cycling, they maintain the initial characteristics. In contrast, there is no visible change to the particles of CS-08 after cycling. On the other hand, the secondary particles of CS-06 are completely

broken down into primary particles. Hence, although CS-06 has better electrochemical charge storage capacity, the capacity retention after cycling is comparatively poor in this case. However, all of the materials retain >60% of the initial specific capacity and 100% of the columbic efficiency after 100 cycles.

Detailed characterization of the electrochemical cells was performed using the electrochemical impedance analysis at charge and discharge states and fitting the derived plots with best fit curves using the suitable equivalent circuit model. Figure 8a shows the fitted Nyquist plots at the charged state [at 4.3 V (versus Li/Li⁺)] for the three materials, and the equivalent circuit is given in the inset. The equivalent circuit consists of three resistance components, such as solution resistance (R_s) , charge-transfer resistance (R_{ct}), and surface resistance (R_1), and two constant phase elements (CPE1 and CPE2), and Warburg impedance (Z_w) . R_{ct} and R_1 are associated with two semicircles in the Nyquist plot and correspond to one CPE and time constant (τ = RC) each. However, in our case, the two semicircles are overlapped into one. 23 From the fitted plots, it is observed that, although CS-06 has slightly higher $R_{\rm s}$, it processes the lowest R_{ct} value among the three. The diffusion behavior of Li⁺ throughout the cathode is determined by analyzing the lowfrequency region (Warburg impedance) of the impedance plot. More precisely, the Li⁺ diffusion coefficient values for all three selected materials are calculated using the slope of the $Z_{\rm re}-\omega^{-0.5}$ plots (Figure 8b) and using the formula given in the Supporting Information. CS-06 shows a diffusion coefficient value of $1.70 \times$ 10^{-10} cm² s⁻¹, which is higher than those of CS-05 and CS-08. The impedance results for the three materials are given in a tabular form (Table 5), and it is observed here that CS-06 is

Table 5. Fitting Results of the Equivalent Circuit and Calculated Diffusion Coefficient Values from the Nyquist Plots of All of the Selected NMC111 Samples

sample	$R_{\rm s}\left(\Omega\right)$	$R_{\mathrm{ct}}\left(\Omega\right)$	$D_{\mathrm{Li}}~(\mathrm{cm^2~s^{-1}})$
CS-05	3.15	13.00	$1.17 (\pm 0.03) \times 10^{-10}$
CS-06	3.19	7.00	$1.70 \ (\pm 0.06) \times 10^{-10}$
CS-08	3.15	12.00	$1.59 (\pm 0.05) \times 10^{-10}$

superior in terms of low $R_{\rm ct}$ and high Li⁺ diffusion coefficient value, which further support its superior electrochemical performance among the three. The impedance profiles for the three materials at the discharged state [at 3.0 V (versus Li/Li⁺)] are shown in Figure S5 of the Supporting Information. It is observed there is a sharp increase in the $R_{\rm ct}$ values after discharge in all of the cases. However, CS-06 shows the lowest $R_{\rm ct}$ value, even at the discharged state, which further confirms that CS-06 is a better cathode material compared to the other two. In the case of CS-06, the high tap density is mainly responsible for higher specific capacity value and the high $I_{(003)}/I_{(104)}$ indicates the lower extent of cation mixing, which determines the facile Li⁺ diffusion and lower charge-transfer resistance throughout the material. The electrochemical performance of CS-06 is comparable to already reported NMC111 (Table 1).

4. CONCLUSION

Theoretical modeling for suitable synthesis conditions of NMC111 through hydroxide co-precipitation and synthesis of the metal hydroxide precursor using low ammonia concentrations to assess the model was demonstrated. The theoretical model was derived from equilibrium constants to optimize the yield when provided with the ammonia concentration and pH

values. Experiments were conducted to assess the model, and the results are accurate for most of the ammonia concentrations. It was also observed that the starting metal ion concentrations had to be adjusted to accommodate the inhomogeneous precipitation of the metal ions at low ammonia concentrations as a result of fast reaction kinetics. Structural characterization of the precursor samples from the experiments showed that samples synthesized at pH \geq 11.5 had a tap density greater than 1 g mL⁻¹, and the analysis of the electron microscopic images showed that all of the precursor samples were made of nanoflaked primary particles that agglomerated to form secondary particles with a size distribution of about 1-60 μ m. Three of the precursor samples with different tap density values were chosen for further electrochemical analysis. The coin cell LIBs are fabricated using selected NMC111 as the cathode. CS-06 with the highest tap density of 1.37 g mL⁻¹ and the highest $I_{(003)}/I_{(104)}$ ratio of 1.45 had the highest specific capacity of 155 mAh g⁻¹ at 0.1 C rate, while CS-08 with the lowest tap density of 0.89 g mL⁻¹ had the lowest specific capacity of 142 mAh g⁻¹. CS-06 is also found to be superior in terms of a higher Li+ diffusion coefficient. All of the samples retained more than 60% of their initial specific capacity at 1 C rate after 100 cycles.

ASSOCIATED CONTENT

Supporting Information

The Supporting Information is available free of charge at https://pubs.acs.org/doi/10.1021/acs.energyfuels.2c01805.

Table of equilibrium constants, starting mass balances of each metal ion concentration and the total ammonia concentration, table of initial experimental conditions and ICP results, plots showing the total product mass using the theoretical model, particle size distribution plots, charge—discharge profiles of CS-05 and CS-08, table with the initial columbic efficiencies, charge—discharge curves at different cycle numbers, pre- and post-cycling SEM images, impedance analysis at the discharged state, and calculation for the Li⁺ diffusion coefficient (PDF)

AUTHOR INFORMATION

Corresponding Authors

Ram B. Gupta — Department of Chemical and Life Science Engineering, College of Engineering, Virginia Commonwealth University, Richmond, Virginia 23284, United States; orcid.org/0000-0002-4385-0799; Email: rbgupta@vcu.edu

Mo Jiang — Department of Chemical and Life Science Engineering, College of Engineering, Virginia Commonwealth University, Richmond, Virginia 23284, United States; Email: mjiang3@vcu.edu

Authors

Jethrine H. Mugumya — Department of Chemical and Life Science Engineering, College of Engineering, Virginia Commonwealth University, Richmond, Virginia 23284, United States; Occid.org/0000-0003-4319-4725

Michael L. Rasche – Department of Chemical and Life Science Engineering, College of Engineering, Virginia Commonwealth University, Richmond, Virginia 23284, United States

Robert F. Rafferty — Department of Chemical and Life Science Engineering, College of Engineering, Virginia Commonwealth University, Richmond, Virginia 23284, United States

- Arjun Patel Department of Chemical and Life Science Engineering, College of Engineering, Virginia Commonwealth University, Richmond, Virginia 23284, United States
- Sourav Mallick Department of Chemical and Life Science Engineering, College of Engineering, Virginia Commonwealth University, Richmond, Virginia 23284, United States
- Mingyao Mou Department of Chemical and Life Science Engineering, College of Engineering, Virginia Commonwealth University, Richmond, Virginia 23284, United States
- Julian A. Bobb Department of Chemical and Life Science Engineering, College of Engineering, Virginia Commonwealth University, Richmond, Virginia 23284, United States

Complete contact information is available at: https://pubs.acs.org/10.1021/acs.energyfuels.2c01805

Notes

The authors declare no competing financial interest.

ACKNOWLEDGMENTS

This material is based on work supported by the U.S. National Science Foundation under Award CMMI-1940948 and the U.S. Department of Energy's Office of Energy Efficiency and Renewable Energy (EERE) under Advanced Manufacturing Office (AMO) Award DE-EE0009110.

REFERENCES

- (1) Zhang, Z.; Zhang, S. S. Challenges of Key Materials for Rechargeable Batteries. In *Rechargeable Batteries*; Springer International Publishing: Cham, Switzerland, 2015; Green Energy and Technology, pp 1–24, DOI: 10.1007/978-3-319-15458-9_1.
- (2) Goodenough, J. B.; Kim, Y. Challenges for Rechargeable Li Batteries. *Chem. Mater.* **2010**, 22 (3), 587–603.
- (3) van Noorden, R. The Rechargeable Revolution: A Better Battery. *Nature.* **2014**, *507*, 26–28.
- (4) Deng, D. Li-Ion Batteries: Basics, Progress, and Challenges. *Energy Sci. Eng.* **2015**, 3 (5), 385–418.
- (5) Sun, X.-G.; Jafta, C. J.; Tan, S.; Borisevich, A.; Gupta, R. B.; Paranthaman, M. P. Facile Surface Coatings for Performance Improvement of NMC811 Battery Cathode Material. *J. Electrochem. Soc.* **2022**, *169* (2), 020565.
- (6) Ellis, B. L.; Lee, K. T.; Nazar, L. F. Positive Electrode Materials for Li-Ion and Li-Batteries. *Chem. Mater.* **2010**, 22 (3), 691–714.
- (7) Dai, Q.; Kelly, J. C.; Gaines, L.; Wang, M. Life Cycle Analysis of Lithium-Ion Batteries for Automotive Applications. *Batteries* **2019**, 5 (2), 48.
- (8) Sun, Y. K.; Myung, S. T.; Park, B. C.; Prakash, J.; Belharouak, I.; Amine, K. High-Energy Cathode Material for Long-Life and Safe Lithium Batteries. *Nat. Mater.* **2009**, *8* (4), 320–324.
- (9) Cairns, E. J.; Albertus, P. Batteries for Electric and Hybrid-Electric Vehicles. *Annu. Rev. Chem. Biomol. Eng.* **2010**, *1* (1), 299–320.
- (10) Jena, K. K.; Alfantazi, A.; Mayyas, A. T. Comprehensive Review on Concept and Recycling Evolution of Lithium-Ion Batteries (LIBs). *Energy Fuels* **2021**, *35* (22), 18257–18284.
- (11) Manthiram, A. A Reflection on Lithium-Ion Battery Cathode Chemistry. *Nat. Commun.* **2020**, *11*, 1550.
- (12) Peralta, D.; Salomon, J.; Colin, J. F.; Boulineau, A.; Fabre, F.; Bourbon, C.; Amestoy, B.; Gutel, E.; Bloch, D.; Patoux, S. Submicronic LiNi_{1/3}Mn_{1/3}Co_{1/3}O₂ Synthesized by Co-precipitation for Lithium Ion Batteries—Tailoring a Classic Process for Enhanced Energy and Power Density. *J. Power Sources* **2018**, 396, 527–532.
- (13) Xia, H.; Luo, Z.; Xie, J. Nanostructured LiMn2O4 and Their Composites as High-Performance Cathodes for Lithium-Ion Batteries. *Prog. Nat. Sci. Mater. Int.* **2012**, 22 (6), 572–584.
- (14) Manthiram, A.; Muraliganth, T. Lithium Intercalation Cathode Materials for Lithium-Ion Batteries. In *Handbook of Battery Materials*, 2nd ed.; Daniel, C., Besenhard, J. O., Eds.; Wiley-VCH Verlag GmbH &

- Co. KGaA: Weinheim, Germany, 2011; Chapter 12, pp 341–375, DOI: 10.1002/9783527637188.ch12.
- (15) Ahmed, S.; Nelson, P. A.; Gallagher, K. G.; Susarla, N.; Dees, D. W. Cost and Energy Demand of Producing Nickel Manganese Cobalt Cathode Material for Lithium Ion Batteries. *J. Power Sources* **2017**, 342, 733–740.
- (16) Ebner, M.; Chung, D.-W.; García, R. E.; Wood, V. Tortuosity Anisotropy in Lithium-Ion Battery Electrodes. *Adv. Energy Mater.* **2014**, 4. 1301278.
- (17) Harris, S. J.; Lu, P. Effects of Inhomogeneities -Nanoscale to Mesoscale -on the Durability of Li-Ion Batteries. *J. Phys. Chem. C* **2013**, 117 (13), 6481–6492.
- (18) Malik, M.; Chan, K. H.; Azimi, G. Effect of Synthesis Method on the Electrochemical Performance of $LiNi_xMnCo_{1-x-y}O_2$ (NMC) Cathode for Li-Ion Batteries: A Review. In *Rare Metal Technology 2021*; Azimi, G., Ouchi, T., Forsberg, K., Kim, H., Alam, S., Baba, A. A., Neelameggham, N. R., Eds.; Springer International Publishing: Cham, Switzerland, 2021; The Minerals, Metals & Materials Series, Vol. 2, pp 37–46, DOI: 10.1007/978-3-030-65489-4 5.
- (19) Zeng, T.; Zhang, C. An Effective Way of Co-precipitating Ni²⁺, Mn²⁺ and Co²⁺ by Using Ammonium Oxalate as Precipitant for Ni-Rich Li-Ion Batteries Cathode. *J. Mater. Sci.* **2020**, *55* (25), 11535–11544.
- (20) Lu, H.; Zhou, H.; Svensson, A. M.; Fossdal, A.; Sheridan, E.; Lu, S.; Vullum-Bruer, F. High Capacity Li[Ni_{0.8}Co_{0.1}Mn_{0.1}]O₂ Synthesized by Sol-Gel and Co-precipitation Methods as Cathode Materials for Lithium-Ion Batteries. *Solid State Ionics* **2013**, 249–250, 105–111.
- (21) Wang, Y.; Roller, J.; Maric, R. Morphology-Controlled One-Step Synthesis of Nanostructured LiNi_{1/3}Mn_{1/3}Co_{1/3}O₂ Electrodes for Li-Ion Batteries. *ACS Omega* **2018**, *3* (4), 3966–3973.
- (22) Lee, M. H.; Kang, Y. J.; Myung, S. T.; Sun, Y. K. Synthetic Optimization of $Li[Ni_{1/3}Co_{1/3}Mn_{1/3}]O_2$ via Co-precipitation. *Electrochim. Acta* **2004**, *50* (4), 939–948.
- (23) Cheng, C.; Drummond, R.; Duncan, S. R.; Grant, P. S. Micro-Scale Graded Electrodes for Improved Dynamic and Cycling Performance of Li-Ion Batteries. *J. Power Sources* **2019**, *413*, 59–67.
- (24) Shui, M.; Gao, S.; Shu, J.; Zheng, W.; Xu, D.; Chen, L.; Feng, L.; Ren, Y. $\text{LiNi}_{1/3}\text{Co}_{1/3}\text{Mn}_{1/3}\text{O}_2$ Cathode Materials for LIB Prepared by Spray Pyrolysis I: The Spectral, Structural, and Electro-Chemical Properties. *Ionics (Kiel)* **2013**, *19*, 41–46.
- (25) Habibi, A.; Jalaly, M.; Rahmanifard, R.; Ghorbanzadeh, M. Solution Combustion Synthesis of the Nanocrystalline NCM Oxide for Lithium-Ion Battery Uses. *Mater. Res. Express* **2018**, *5*, 025506.
- (26) Dong, H.; Koenig, G. M. A Review on Synthesis and Engineering of Crystal Precursors Produced: Via Coprecipitation for Multicomponent Lithium-Ion Battery Cathode Materials. *CrystEngComm* **2020**, 22 (9), 1514–1530.
- (27) Yoon, J. H.; Bang, H. J.; Prakash, J.; Sun, Y. K. Comparative Study of Li[Ni_{1/3}Co_{1/3}Mn_{1/3}]O₂ Cathode Material Synthesized via Different Synthetic Routes for Asymmetric Electrochemical Capacitor Applications. *Mater. Chem. Phys.* **2008**, *110* (2–3), 222–227.
- (28) Hu, C. Y.; Guo, J.; Du, Y.; Xu, H. H.; He, Y. H. Effects of Synthesis Conditions on Layered Li $[Ni_{1/3}Co_{1/3}Mn_{1/3}]O_2$ Positive-Electrode via Hydroxide Co-precipitation Method for Lithium-Ion Batteries. *Trans. Nonferrous Met. Soc. China (English Ed.* **2011**, 21 (1), 114–120.
- (29) Hy, S.; Liu, H.; Zhang, M.; Qian, D.; Hwang, B. J.; Meng, Y. S. Performance and Design Considerations for Lithium Excess Layered Oxide Positive Electrode Materials for Lithium Ion Batteries. *Energy Environ. Sci.* **2016**, 9 (6), 1931–1954.
- (30) Tian, H.; Ye, N.; Liu, D.; Li, W. Effects of Synthesis Conditions on the Structural and Electrochemical Properties of Layered LiNi_{1/3}Co_{1/3}Mn_{1/3}O₂ Cathode Material via Oxalate Co-precipitation Method. *Rare Met.* **2008**, *27* (6), 575–579.
- (31) Deng, C.; Liu, L.; Zhou, W.; Sun, K.; Sun, D. Effect of Synthesis Condition on the Structure and Electrochemical Properties of Li[Ni_{1/3}Mn_{1/3}Co_{1/3}]O₂ Prepared by Hydroxide Co-precipitation Method. *Electrochim. Acta* **2008**, 53 (5), 2441–2447.
- (32) Shen, Y.; Wu, Y.; Xue, H.; Wang, S.; Yin, D.; Wang, L.; Cheng, Y. Insight into the Coprecipitation-Controlled Crystallization Reaction

- for Preparing Lithium-Layered Oxide Cathodes. ACS Appl. Mater. Interfaces 2021, 13, 717-726.
- (33) Van Bommel, A.; Dahn, J. R. Analysis of the Growth Mechanism of Coprecipitated Spherical and Dense Nickel, Manganese, and Cobalt-Containing Hydroxides in the Presence of Aqueous Ammonia. *Chem. Mater.* **2009**, *21*, 1500–1503.
- (34) Yang, Y.; Xu, S.; Xie, M.; He, Y.; Huang, G.; Yang, Y. Growth Mechanisms for Spherical Mixed Hydroxide Agglomerates Prepared by Co-precipitation Method: A Case of Ni_{1/3}Co_{1/3}Mn_{1/3}(OH)₂. *J. Alloys Compd.* **2015**, *619*, 846–853.
- (35) Hua, W.; Liu, W.; Chen, M.; Indris, S.; Zheng, Z.; Guo, X.; Bruns, M.; Wu, T. H.; Chen, Y.; Zhong, B.; Chou, S.; Kang, Y. M.; Ehrenberg, H. Unravelling the Growth Mechanism of Hierarchically Structured Ni_{1/3}Co_{1/3}Mn_{1/3}(OH)₂ and Their Application as Precursors for High-Power Cathode Materials. *Electrochim. Acta* 2017, 232, 123–131.
- (36) Smith, J. N.; Keil, A. D.; Noll, R. J.; Cooks, R. G. Ion/Molecule Reactions for Detecting Ammonia Using Miniature Cylindrical Ion Trap Mass Spectrometers. *Analyst* **2011**, *136*, 120–127.
- (37) Xu, L.; Zhou, F.; Kong, J.; Chen, Z.; Chen, K. Synthesis of Li(Ni_{0.6}Co_{0.2}Mn_{0.2})O₂ with Sodium DL-Lactate as an Eco-Friendly Chelating Agent and Its Electrochemical Performances for Lithium-Ion Batteries. *Ionics (Kiel)*. **2018**, 24 (8), 2261–2273.
- (38) Kong, J. Z.; Yang, X. Y.; Zhai, H. F.; Ren, C.; Li, H.; Li, J. X.; Tang, Z.; Zhou, F. Synthesis and Electrochemical Properties of Li-Excess Li_{1+x}[Ni_{0.5}Co_{0.2}Mn_{0.3}]O₂ Cathode Materials Using Ammonia-Free Chelating Agent. *J. Alloys Compd.* **2013**, *580*, 491–496.
- (39) Wittrig, S. Ammonia Fuel Opportunities, Markets, Issues. Workshop on Bridging Renewable Electricity with Transportation Fuels; Denver, CO, Aug 27–28, 2015; https://arpa-e.energy.gov/sites/default/files/Wittrig_Ammonia_TransportationFuels_Workshop.pdf (accessed May 26, 2022).
- (40) Wagner, A. C.; Bohn, N.; Geßwein, H.; Neumann, M.; Osenberg, M.; Hilger, A.; Manke, I.; Schmidt, V.; Binder, J. R. Hierarchical Structuring of NMC111-Cathode Materials in Lithium-Ion Batteries: An In-Depth Study on the Influence of Primary and Secondary Particle Sizes on Electrochemical Performance. ACS Appl. Energy Mater. 2020, 3 (12), 12565–12574.
- (41) Feng, Z.; Barai, P.; Gim, J.; Yuan, K.; Wu, Y. A.; Xie, Y.; Liu, Y.; Srinivasan, V. In Situ Monitoring of the Growth of Nickel, Manganese, and Cobalt Hydroxide Precursors during Co-precipitation Synthesis of Li-Ion Cathode Materials. *J. Electrochem. Soc.* **2018**, *165* (13), A3077.
- (42) Zhang, S.; Deng, C.; Yang, S. Y.; Niu, H. An Improved Carbonate Co-precipitation Method for the Preparation of Spherical Li-[Ni_{1/3}Co_{1/3}Mn_{1/3}]O₂ Cathode Material. *J. Alloys Compd.* **2009**, 484 (1–2), 519–523.
- (43) Kim, S.; Park, S.; Jo, M.; Beak, M.; Park, J.; Jeong, G.; Yu, J. S.; Kwon, K. Electrochemical Effects of Residual Al in the Resynthesis of $\text{Li}[\text{Ni}_{1/3}\text{Mn}_{1/3}\text{Co}_{1/3}]\text{O}_2$ Cathode Materials. *J. Alloys Compd.* **2021**, 857, 157581.
- (44) Yv, L.; Wang, J.; Li, X.; Dai, L.; Shao, Z. Preparation and Electrochemical Properties of Ti-Doped LiNi_{1/3}Co_{1/3}Mn_{1/3}O₂ Cathode Materials via Co-precipitation Route. *Ionics* **2021**, *27*, 3769–3776.
- (45) Abram, C.; Shan, J.; Yang, X.; Yan, C.; Steingart, D.; Ju, Y. Flame Aerosol Synthesis and Electrochemical Characterization of Ni-Rich Layered Cathode Materials for Li-Ion Batteries. ACS Appl. Energy Mater. 2019, 2, 1319–1329.
- (46) Shen, Y.; Xue, H.; Wang, S.; Zhang, D.; Yin, D.; Wang, L.; Cheng, Y. Ammonia-Low Coprecipitation Synthesis of Lithium Layered Oxide Cathode Material for High-Performance Battery. *Chem. Eng. J.* **2021**, *411*, 128487.
- (47) Wang, D.; Belharouak, I.; Zhou, G.; Amine, K. Nanoarchitecture Multi-Structural Cathode Materials for High Capacity Lithium Batteries. *Adv. Funct. Mater.* **2013**, 23 (8), 1070–1075.
- (48) van Bommel, A.; Dahn, J. R. Synthesis of Spherical and Dense Particles of the Pure Hydroxide Phase $Ni_{1/3}Mn_{1/3}Co_{1/3}(OH)_2$. *J. Electrochem. Soc.* **2009**, *156* (5), A362.
- (49) Park, S. H.; Kang, S. H.; Belharouak, I.; Sun, Y. K.; Amine, K. Physical and Electrochemical Properties of Spherical

- $\text{Li}_{1+x}(\text{Ni}_{1/3}\text{Co}_{1/3}\text{Mn}_{1/3})_{1-x}\text{O}_2$ Cathode Materials. J. Power Sources **2008**, 177 (1), 177–183.
- (50) Yabuuchi, N.; Koyama, Y.; Nakayama, N.; Ohzuku, T. Solid-State Chemistry and Electrochemistry of LiCo_{1/3}Ni_{1/3}Mn_{1/3}O₂ for Advanced Lithium-Ion Batteries. *J. Electrochem. Soc.* **2005**, *152* (7), A1434.
- (51) Yabuuchi, N.; Ohzuku, T. Novel Lithium Insertion Material of LiCo_{1/3}Ni_{1/3}Mn_{1/3}O₂ for Advanced Lithium-Ion Batteries. *J. Power Sources* **2003**, *119*–*121*, 171–174.
- (52) Zheng, Z.; Guo, X. D.; Chou, S. L.; Hua, W. B.; Liu, H. K.; Dou, S. X.; Yang, X. S. Uniform Ni-Rich LiNi_{0.6}Co_{0.2}Mn_{0.2}O₂ Porous Microspheres: Facile Designed Synthesis and Their Improved Electrochemical Performance. *Electrochim. Acta* **2016**, *191*, 401–410.
- (53) Choi, Y. M.; Pyun, S. II; Moon, S. I. Effects of Cation Mixing on the Electrochemical Lithium Intercalation Reaction into Porous Li _{1-z}Ni_{1-y}Co_vO₂ Electrodes. *Solid State Ionics* **1996**, 89 (1-2), 43-52.
- (54) Wang, M.; Chen, Y.; Wu, F.; Su, Y.; Chen, L.; Wang, D. Characterization of Yttrium Substituted LiNi_{0.33}Mn_{0.33}Co_{0.33}O₂ Cathode Material for Lithium Secondary Cells. *Electrochim. Acta* **2010**, *55* (28), 8815–8820.
- (55) Wang, D.; Belharouak, I.; Ortega, L. H.; Zhang, X.; Xu, R.; Zhou, D.; Zhou, G.; Amine, K. Synthesis of High Capacity Cathodes for Lithium-Ion Batteries by Morphology-Tailored Hydroxide Coprecipitation. *J. Power Sources* **2015**, 274, 451–457.

□ Recommended by ACS

Mechanical Pulverization of Co-Free Nickel-Rich Cathodes for Improved High-Voltage Cycling of Lithium-Ion Batteries

Ryan Brow, Arumugam Manthiram, et al.

JUNE 08, 2022

ACS APPLIED ENERGY MATERIALS

READ 🗹

Morphological Evolution and Solid–Electrolyte Interphase Formation on LiNi $_{0.6}$ Mn $_{0.2}$ Co $_{0.2}$ O $_{2}$ Cathodes Using Highly Concentrated Ionic Liquid Electrolytes

Meisam Hasanpoor, Patrick C. Howlett, et al.

MARCH 11, 2022

ACS APPLIED MATERIALS & INTERFACES

READ 🗹

Improved High Voltage Performance of Li-ion Conducting Coated Ni-rich NMC Cathode Materials for Rechargeable Li Battery

Himani Gupta, Rajendra Kumar Singh, et al.

NOVEMBER 28, 2021

ACS APPLIED ENERGY MATERIALS

READ **C**

Effect of ${\rm TiO}_x$ Surface Modification on the Electrochemical Performances of Ni-Rich (NMC-622) Cathode Material for Lithium-Ion Batteries

Satish Kumar MYLAVARAPU, An Hardy, et al.

SEPTEMBER 27, 2021

ACS APPLIED ENERGY MATERIALS

READ 🗹

Get More Suggestions >